Progress in Additive Manufacturing
https://doi.org/10.1007/s40964-026-01813-6

RESEARCH

A convergent manufacturing pathway for smart metallic structures with embedded sensing

Jinhan Ren[1] · Shinan Huang[1] · Sazedur Rahman[1] · Peiyuan Zhou[1] · Yiming Fan[1] · Brandon Villanueva[1] · Glenn Saunders[1,2] · John Wen[2,3] · Sandipan Mishra[1,2] · Johnson Samuel[1,2] · Fotis Kopsaftopoulos[1,2] · Semih Akin[1,2]

Received: 31 March 2026 / Accepted: 4 June 2026

Abstract

Smart metallic structures (SMS) with embedded sensors are gaining significant interest as they enable real-time sensing and structural monitoring in mission-critical applications. However, integrating sensors directly into metallic materials remains challenging due to the extreme thermal loads and metallurgical incompatibilities inherent to metal additive manufacturing (MAM). To address this gap, this study introduces a convergent manufacturing pathway that integrates wirearc additive manufacturing (WAAM), subtractive machining, ceramic sensor shielding, and cold spray metallization to realize smart metallic structures with fully embedded sensing capabilities. The developed sensor encapsulation approach, combining ceramic shielding with cold spray metallization, enables seamless WAAM deposition over the sensor regions and allows the embedding of commercial off-the-shelf (COTS) sensors in structural aluminum alloy beams (Al-5356), resulting in fully functional smart beams. Unlike prior studies that typically demonstrate a single sensing modality with single-sensor embedding, this work integrates a dense multi layer and multi modal sensor network featuring multiple sensor configurations within a standard bending beam footprint (180 mm × 20 mm × 13 mm). This represents a significant advancement in both sensor density and integration fidelity for MAM. Comprehensive thermal and mechanical experiments confirm that the embedded sensors remain fully functional and accurate throughout testing. The temperature sensors (RTDs) capture both steady-state and transient thermal responses with less than 2.2% error, while the strain gauges provide high-fidelity measurements with deviations below 2.5%. Furthermore, the fabricated smart beams exhibit a mechanical debit of less than 11% under static bending and less than 20% under dynamic bending relative to baseline beams without embedded sensors, while maintaining full structural and sensing integrity. This work establishes a convergent manufacturing pathway that enables reliable sensor embedding under the demanding conditions of MAM and marks a significant step toward next-generation SMS.

Keywords Smart metallic structures · Embedded sensors · Embedded intelligence · Additive manufacturing · Convergent manufacturing · Structural health monitoring · Cold spray · Wire arc additive manufacturing (WAAM)

List of symbols

Symbols

A	RTD coefficient A
B	RTD coefficient B
b	Width of specimen
D	Mid-span deflection
d	Depth of specimen
L	Support span
N_f	Fatigue life
P	Load
R	Flexural strength
$R(T)$	Resistance at temperature T
T	Temperature
y_1	Neutral axis to surface
y_2	Neutral axis to embedded SG
Z	Maximum load

Greek letters

α	RTD linear coefficient

Extended author information available on the last page of the article

β RTD linear coefficient
σ Stress
ϵ Flexural strain
ϵ_1 Surface strain
ϵ_2 Embedded SG equivalent strain

Abbreviations

Al	Aluminum
ASTM	American Society for Testing and Materials
CNC	Computer numerical control
COTS	Commercial off-the-shelf
CS	Cold spray
FPCB	Flexible printed circuit board
MAM	Metal additive manufacturing
PZT	Piezoelectric transducer
RTD	Resistance temperature detector
SEM	Scanning electron microscope
SG	Strain gauge
SHM	Structural health monitoring
SMS	Smart metallic structure
SW	Spot weld
TC	Thermocouple
WAAM	Wire arc additive manufacturing

1 Introduction

Smart structures are structural components integrated with sensors that enable continuous monitoring of structural health, environmental conditions, and operating states [1]. These systems facilitate real-time data acquisition and analysis, thereby enhancing safety, performance, and reliability [2–4]. In recent years, growing interest in embedding sensors within metallic components has driven the development of smart metallic structures (SMS) [5, 6], which have found broad applicability across aerospace [7], defense [8], automotive [9], robotics [10], and energy systems [11]. This interest is driven by several key factors: (i) metals dominate load-bearing structures in safety-critical systems [12]; (ii) there is a need for in-situ sensing within metallic components operating under demanding conditions [13]; and (iii) there is growing demand for high-fidelity, non-destructive structural monitoring without compromising mechanical integrity or functionality [14].

In this context, metal additive manufacturing (MAM) technologies offer a promising pathway for realizing SMS by enabling the fabrication of structures with enhanced design freedom and precise process control. Owing to these capabilities, MAM technologies facilitate the integration of sensors within metallic components during fabrication, enabling precise sensor placement, multi-material architectures, and tailored microstructures. Hence, MAM-based approaches have emerged as a promising platform for producing next-generation SMS with enhanced functionality, robustness, and scalability [15]. Over the last decade, several MAM techniques have been proposed to integrate sensors into metallic structures [16]. These approaches primarily include powder bed fusion (PBF) [17–19], directed energy deposition (DED) [13, 20, 21], and ultrasonic additive manufacturing (UAM) [22–24], each offering distinct advantages in terms of sensor embedding strategies, material compatibility, and process integration. Collectively, these efforts have significantly advanced the development of additively manufactured SMS. A recent review by Rahman et al. [16] summarizes the state-of-the-art in SMS with embedded sensing.

Despite significant advances, critical challenges remain, including sensor survivability under thermal exposure during fabrication, reliable interfacial adhesion between dissimilar and inhomogeneous layers, and overall scalability [16, 25–27]. Moreover, real-world deployment of SMS requires reliable field measurements such as temperature and strain rather than isolated single-point sensing. This necessitates the integration of distributed, multi modal sensor networks capable of coupled measurements, as opposed to reliance on a single embedded sensor. Taken together, these challenges underscore the need for innovative manufacturing approaches that enable seamless embedding of dense, multi modal sensor networks within metallic structures without compromising sensing fidelity and structural integrity.

Most recently, the authors' group has pioneered the use of wire arc additive manufacturing (WAAM) as a primary MAM platform for fabricating SMS with subsurface embedded sensors [28, 29]. This approach enabled the embedding of sensing elements beneath the metal surface skin, facilitating the integration of distributed sensor networks. Despite its promise, this approach relied on machining sensor pockets and remained limited to subsurface embedding rather than achieving fully embedded sensors within the metallic structure. Bypassing sensor-cavity machining is particularly critical for preserving mechanical integrity, as machined cavities act as stress concentrators, especially in architectures involving dense sensor networks. Moreover, achieving fully embedded sensor networks requires seamless resumption of WAAM deposition over sensor regions, which remains a key technical challenge.

To address these critical gaps and build on our preliminary work [28, 29], this study introduces a convergent manufacturing pathway that integrates WAAM, subtractive machining (surface facing), ceramic shielding, and cold spray (CS) metallization to realize SMS with fully embedded sensing capabilities. A sensor encapsulation strategy combining ceramic shielding and CS metallization is developed, eliminating the need for sensor-cavity machining. The electrically conductive CS metallization on ceramic shielding enables seamless resumption of WAAM deposition over sensor-packaged regions, effectively mitigating wire-arc instabilities. Multilayer dense sensor networks composed of commercial off-the-shelf (COTS) temperature and strain sensors are embedded within two distinct layers of a standard bending-beam footprint (180 mm × 20 mm × 13 mm). Each layer incorporates a dense sensor network comprising resistive temperature detectors (RTDs) and strain gauges (SGs) within the standard beam footprint. To the best of our knowledge, this is the first demonstration of multi-layer, multimodal temperature-and-strain sensor networks embedded within metal additively manufactured components. Comprehensive microstructural analyses, together with thermal and mechanical experiments, are conducted to assess interfacial bonding, sensor integrity, sensing fidelity, and the structural performance of the resulting smart beams.

The remainder of this manuscript is organized as shown in Fig. 1. Section 2 introduces the proposed convergent manufacturing pathway for fabricating SMS. Section 3 describes the sensor network, embedding strategy, and microstructural characterization of the resulting smart structures (i.e., smart beams). Section 4 presents comprehensive structural monitoring evaluations, including thermal, mechanical, and coupled thermo-mechanical testing. Finally, Sect. 5 discusses the potential areas for improvement, while Sect. 6 summarizes the key findings and outlines future research directions.

2 Convergent manufacturing of smart metallic structures

Figure 2a illustrates the developed convergent manufacturing pathway for embedding functional sensors within additively manufactured metal structures. As depicted in Fig. 2a, the pathway consists of six sequential steps: (1) robotic WAAM to fabricate the host structure (Fig. 2b); (2) surface preparation for sensor attachment, including machining (facing) and sandblasting; (3) sensor integration; (4) application of a ceramic shielding layer; (5) surface metallization via robotic cold spray (Fig. 2c); and (6) resumption of WAAM deposition to realize the SMS with fully embedded sensors. The following subsections describe each step in detail, and Table 1 summarizes the operational settings for each process. Representative images of each step are also provided in the Supporting Information (Fig. S1).

2.1 (Step 1) WAAM to build the host structure

The fabrication process begins with constructing the host metal structure (Al-5356) using WAAM, which serves as the backbone of the proposed convergent manufacturing pathway. WAAM was employed owing to its high deposition rate, excellent metallurgical bonding, and relatively low material waste compared to other AM processes such as powder bed fusion and laser powder DED [30]. In addition, the use of Al-5356 alloy provides a favorable combination of strength, ductility, and corrosion resistance [31], making it well suited for structural components in SMS applications. To enhance deposition–substrate bonding, the build was deposited onto an Al-6061 build plate featuring machined surface grooves (see Fig. S2 and Video S1 in the Supporting Information), which increased surface roughness and promoted stronger metallurgical adhesion between the first layer and the build plate.

Subsequently, the WAAM process was carried out using the robotic system shown in Fig. 2b, enabling precise control over deposition [32, 33]. The wire was fed into the torch at a rate of 0.17 m/s, while the torch traversed at 4 mm/s (Table 1). The host build (length: 240 mm, width: 70 mm, height: 18 mm) was fabricated in three WAAM layers, each comprising 20 beads with 3 mm layer-hatch spacing (see Video S1, Supporting Information). To promote in-layer surface flatness and geometric uniformity, adjacent WAAM beads were deposited using a conventional

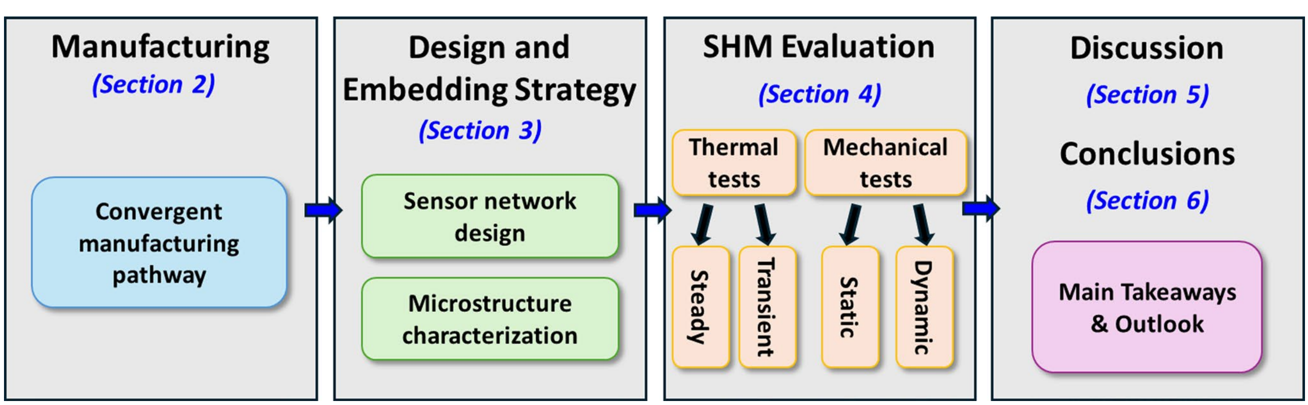

Fig. 1 Schematic overview of the workflow and overall structure of the present work

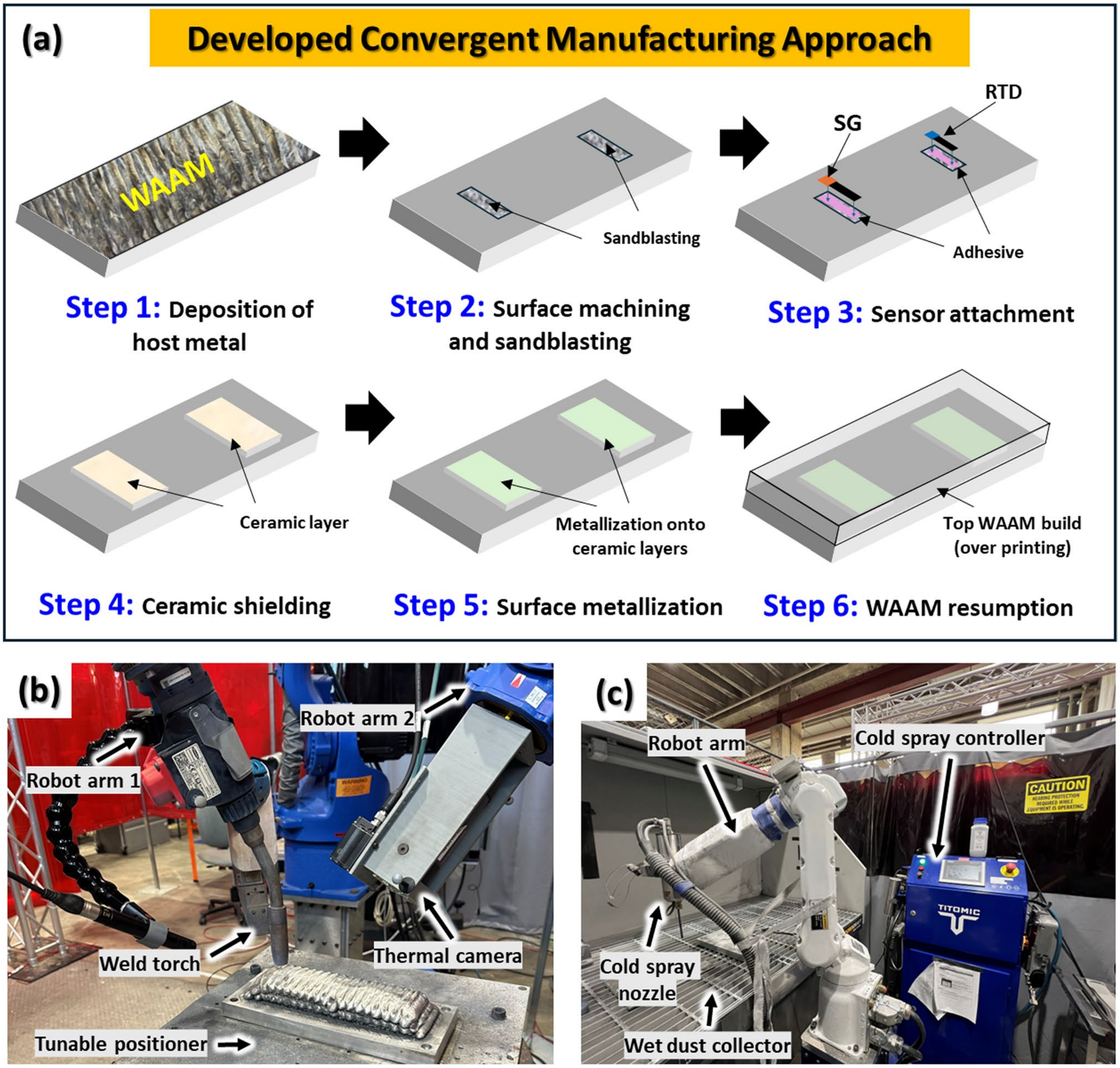

Fig. 2 Developed convergent manufacturing pathway: **a** Schematic illustration of the overall approach; representative images of the robotic **b** WAAM setup and **c** Cold spray setup

bidirectional back-and-forth strategy. Following deposition, high-pressure compressed air was used to clean the surface and remove spatter and other contaminants before the next processing step.

2.2 (Step 2) Surface preparation

Following deposition of the host structure, surface facing was performed via CNC milling to remove weld-induced roughness and produce a uniform, flat surface for subsequent sensor attachment. The facing operation was conducted off-line using a three-axis CNC milling machine (*HAAS, Model: TM-2*). After the initial WAAM build, the part was removed from the WAAM cell and transferred to the CNC machine for surface finishing. Notably, machining was used solely for surface facing of the WAAM-built layer to facilitate sensor attachment on a smooth surface, and no sensor-cavity machining was performed. Sandblasting with 64-grit aluminum oxide medium was applied to the as-machined surface at the 12 mm × 6 mm sensor locations, using an aluminum mask to create micro-roughness for improved sensor bonding (see Step 2 in Fig. S1, Supporting Information).

Table 1 Operational settings for each process

Fabrication Process	Parameter	Settings
Step 1 WAAM for host structure	Material	Aluminum alloy (Al-5356)
	Wire feed rate	400 inch/min (~ 0.17 m/s)
	Torch speed	4 mm/s
	Number of weld beads	20
	Bead (hatch) distance	6 mm
	Arc-on temperature	140–150 °C
Step 2 Surface preparation	Cutting tool	3.175 mm ball end mill
	Spindle speed	4,000 rpm
	Feed rate	2 inch/min (~50.8 mm/min)
	Sandblasting	64-grit aluminum oxide
Step 3 Sensor integration	RTD SW voltage/current	170 V / 20 kA
	SG SW voltage/current	130 V / 35 kA
	Bonding agent	M-Bond 610 adhesive
	Oven curing temperature	175 °C for 1 h + 300 °C for 2 h
Step 4 Ceramic shielding	Air-curing humidity	40–50%
	Air-curing time	24 h
Step 5 Cold spray metallization	Material	Mixture of Al, Al_2O_3, and Zn
	Gas temperature	400 °C
	Gas pressure	6 bar (0.6 MPa)
	Nozzle traverse speed	20 mm/s
	Nozzle stand-off distance	25 mm
Step 6 WAAM resumption	–	Same as Step 1

2.3 (Step 3) Sensor integration

In this work, commercial off-the-shelf (COTS) sensors were employed, including strain gauges (SGs, *Omega, SGT-2/350-XY43*) and resistance temperature detectors (RTDs, *Omega, 5RTD-F3100*), which were used as procured. Figure 3a shows both sensor types along with their respective footprints. The RTDs used in this study have an operating temperature range of −50 to 500 °C [34], making them inherently compatible with the subsequent manufacturing steps. In contrast, the selected SGs have a lower operating range of -75–200 °C [35], which is below the peak temperatures encountered during WAAM over-deposition. Hence, ceramic encapsulation is necessary to thermally protect the SGs during processing. Although high-temperature SGs (e.g., free-filament and spot-weldable metal-backed gauges) are commercially available, these sensors are typically larger in footprint and require complex installation procedures (e.g., spot welding, specialized surface preparation, high-temperature bonding). Consequently, their integration into compact embedded sensing architecture is challenging, particularly for the dense multilayer sensor network targeted in this study. As such, the thin-film COTS SGs (see Fig. 3a) were selected to minimize encapsulation volume while achieving the desired sensing and structural performance, as well as enabling high sensor density within the standard bending beam geometry.

Prior to attaching the sensors to the host structure, flexible printed circuit board (FPCB) packaging was applied to each sensor to provide mechanical support, protect the sensing elements during handling, and facilitate reliable electrical interfacing (see Fig. 3b). This packaging also improves durability during subsequent processing steps by mitigating strain concentrations at the sensor terminals and ensuring stable signal transmission. The sensor electrodes were spot-welded (*UNITEK thin-line spot welder*) to ensure robust electrical connections and minimize contact resistance. Video S2 (Supporting Information) shows the spot-welding process used for sensor–FPCB integration. Lastly, the packaged sensors were directly bonded to the surface of the host structure using *M-Bond 610* adhesive. This adhesive was selected for its high-temperature stability, strong shear strength, and compatibility with both SGs and RTDs, ensuring reliable adhesion during subsequent WAAM deposition and thermal cycling [36]. To cure the adhesive, the sensor-attached structure underwent a two-stage thermal cycle: one hour at 175 °C followed by two hours at 300 °C.

Although the second curing stage exceeded the recommended operating temperature range of the selected SGs (i.e., -75–200 °C), this does not necessarily imply sensor failure, as the specified range primarily refers to guaranteed measurement fidelity rather than structural survival. Electrical resistance measurements before and after curing (see Fig. S3, Supporting Information) showed no open circuit or abnormal resistance shift, indicating that the SGs remained functional following both the adhesive curing process and subsequent WAAM thermal exposure. After curing, the specimens were allowed to cool naturally to room temperature under ambient conditions.

2.4 (Step 4) Ceramic shielding

To protect the sensors from direct thermal exposure during WAAM deposition, a 1 mm-thick ceramic shielding layer was applied over the sensor assemblies to serve as an effective thermal barrier. In this context, a zirconia-based ceramic slurry paste was applied to ensure uniform coverage and robust thermal insulation. The paste was deposited onto the sensor assemblies (i.e., sensors with FPCB packaging) through manual dispensing using a 17-gauge syringe, enabling controlled placement and consistent thickness with the aid of a masking fixture (see Step 4 in Fig. S1, Supporting Information). The ceramic was applied beyond the sensor footprint, covering a total area of 14 mm × 6 mm for

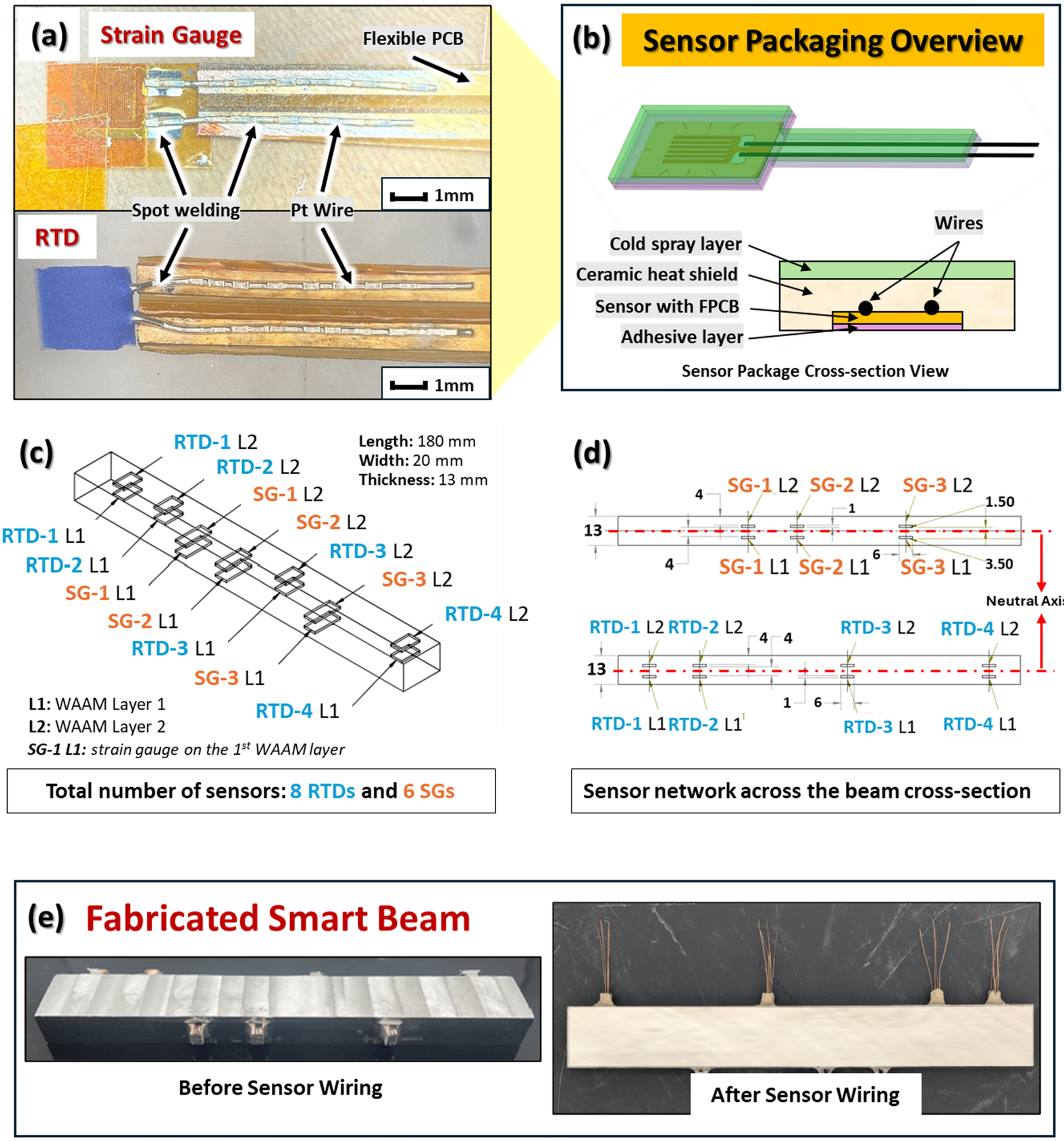

Fig. 3 Sensor packaging and smart beam design: **a** Representative images of the SG (top) and RTD (bottom) sensors with FPCB packaging; **b** Schematic overview of sensor packaging within the metallic structure; **c** Smart beam design featuring two layers of sensor networks (each layer includes 4 RTDs and 3 SGs, for a total of 14 embedded sensors); **d** Technical drawing of the beam showing the sensor layout and its distance from the neutral axis; and **e** Representative images of the fabricated beams before wiring (left) and after wiring (right)

SGs and 10 mm × 6 mm for RTDs, to ensure reliable bonding across both the sand-blasted metal region of the host structure and the sensor array. Extending the ceramic layer in this manner improves mechanical anchoring during over-deposition, enhances load transfer across the interface, and prevents delamination or edge lifting that could occur if the ceramic were confined strictly to the sensor footprint. As such, this approach eliminated the need for cavity machining and enabled sensor embedding without introducing significant stress concentrators. The applied ceramic layer limits heat transfer to the embedded sensors, preventing thermal degradation, sensor drift, or failure during subsequent metal deposition. Following application, the ceramic was cured at room temperature for 24 h, forming a green body with sufficient mechanical strength and dimensional stability to withstand the thermal and mechanical conditions of the over-deposition process.

2.5 (Step 5) Cold spray metallization

For seamless resumption of WAAM deposition over the sensor-embedded regions, a continuous electrically conductive pathway is essential to maintain arc stability and prevent process interruptions. However, the ceramic shielding layer is intrinsically insulating, necessitating the creation of a conductive intermediary layer to support stable arc initiation and propagation. To address this requirement, CS metallization was employed to deposit a dense, electrically conductive thin-film coating (198 ± 55 μm) onto the ceramic surface. In this step, a mixture of metallic feedstock powders ($Al + Al_2O_3 + Zn$) was sprayed using a robotic low-pressure CS system (*Titomic D523*) (Fig. 2c) to create a conformal, mechanically robust, and electrically continuous surface. The particle morphology and size distribution of the feedstock powders are provided in Fig. S4 (Supporting Information), and the corresponding operational settings used for CS deposition are summarized in Table 1. The metallized layer, achieved using a single spray pass, provides sufficient electrical conductivity for stable WAAM over-deposition and strong mechanical anchoring for subsequent WAAM layers, thereby facilitating uninterrupted fabrication of the SMS. Figure 3b schematically illustrates the sensor packaging configuration, highlighting the sequential arrangement of protective, functional, and structural layers that collectively ensure sensor survivability, electrical connectivity, and seamless integration within the SMS architecture.

2.6 (Step 6) WAAM resumption

WAAM deposition was seamlessly resumed over the sensor-bonded and packaged host structure to fully integrate the sensor networks (see Fig. 3c, d) within the build. Upon completing the WAAM process, the structure underwent final surface machining to achieve a near-net-shape beam geometry, as shown in Fig. 3e (left panel). Finally, the embedded sensors were wired out through designated routing paths for signal acquisition and functional verification (Fig. 3e, right panel), enabling subsequent structural testing of the fabricated SMS. Collectively, by leveraging the convergent manufacturing pathway developed in this work, dense sensor networks of COTS strain and temperature sensors were integrated within a WAAM-built beam, as detailed in the following section.

3 Sensor network and embedding strategy

As illustrated in Fig. 3c, a two-layer sensor network, with each layer comprising four RTDs and three SGs, was embedded within an ASTM-standard bending beam [37] (180 mm × 20 mm × 13 mm). A detailed technical drawing of the complete sensor network layout is also provided in Fig. S5 (Supporting Information). This multilayer, densely distributed sensor network was selected to capture the temperature and strain evolution throughout the beam rather than relying on single-point local measurement. This design enables higher sensing resolution and provides richer diagnostic capability for structural evaluation. From a manufacturing perspective, the sensor spacing and layout were constrained by WAAM process considerations. To maintain adequate thermal control between adjacent weld beads, the minimum center-to-center spacing between embedded sensors was set to no less than 15 mm. Under these constraints, the 14-sensor layout was designed to achieve dense sensor embedding within the available beam volume while preserving manufacturability. It should be noted that the exact number and spatial distribution of embedded sensors can be readily adapted to meet specific experimental objectives and process requirements. Figures S5–S6 (Supporting Information) present the sensor network designs used for the tests described in Sect. 4, highlighting the flexibility of the proposed embedding strategy.

In all sensor-network designs, the SGs were strategically embedded asymmetrically with respect to the neutral axis, i.e., 3.5 mm away in Layer 1 and 1.5 mm away in Layer 2 (Fig. 3d and Figs. S5–S7), to assess strain sensitivity, gradient response, and measurement fidelity of embedded sensors under bending-dominated loading. The RTDs were also positioned at corresponding locations within each layer to capture through-thickness temperature gradients and support coupled thermo-mechanical analysis of the developed smart structure.

All sensors were first spot-welded onto the FPCB for packaging, after which the assembled sensors were bonded onto the pre-treated beam surface (see Video S2 in the Supporting Information). This sequential approach ensured robust electrical connections, proper alignment, and reliable mechanical anchoring prior to ceramic shielding and subsequent CS metallization. In addition, the use of an FPCB provided a flexible and stable platform for routing sensor leads, minimizing wiring clutter, and protecting junctions during handling. This integrated packaging and bonding strategy is essential for maintaining sensor integrity throughout the subsequent ceramic encapsulation and metal deposition steps.

To interface the embedded sensor network with dedicated data acquisition modules (*National Instruments NI-9216 for*

RTDs and NI-9235 for SGs), side tabs were incorporated into the beam design to expose the FPCB leads, facilitating electrical connections (Fig. 3d and Figure S8 (Supporting Information). These tabs were created by off-line machining of dedicated recesses along the beam edges after WAAM resumption, allowing the FPCB leads to be safely routed outward without interfering with the surrounding metal regions (Fig. 3e, left panel, and Video S3 in the Supporting Information). Finally, external copper wires (28-gauge, approximately 320 μm) were soldered to the exposed tabs to establish reliable electrical connections between the embedded sensors and the data acquisition system (Fig. 3e, right panel). This configuration provides secure access to the sensor terminals while preserving the structural integrity of the smart structure.

3.1 Microstructural characterization

To evaluate the reliability of the proposed manufacturing pathway prior to structural evaluation, the microstructure of the resulting deposition was examined. As shown in Fig. 4a, two regions of interest were selected and sectioned for cross-sectional analysis. Region A–A is oriented in the transverse direction of the fabricated beam—perpendicular to the beam length—with the cutting location positioned directly adjacent to the embedded sensor. Region B–B, on the other hand, is orthogonal to the WAAM printing direction but parallel to the beam length, enabling examination along the WAAM deposition direction. Both sectional surfaces were hot-mounted using bakelite and then sequentially polished with abrasive sandpapers (grits 240, 400, 600, and 1200) to expose the embedded sensor cross-section. Finally, smooth mirror-polished surfaces were obtained by micron-scale polishing with 15 μm abrasive media for microscopy analysis.

Figure 4b shows an optical microscopy image of Section A–A, highlighting the additively manufactured region with the embedded sensor and its encapsulation. The layer-by-layer WAAM deposition was successfully achieved without delamination or significant porosity at the WAAM–WAAM interface, confirming interlayer fusion. Notably, the interface between the WAAM and the cold-sprayed layer exhibits successful resumption of WAAM deposition on the metallized ceramic surface, as shown in Fig. 4b. However, local voids were observed at the sharp corner of the ceramic–CS–WAAM interface. These localized defects are primarily attributed to the geometric discontinuities introduced during the ceramic shielding step. As shown in Fig. S1 (Step 4) in the Supporting Information, the ceramic slurry was deposited within a clay mask, producing a shielding layer with vertical sidewalls and sharp corners after drying. During the subsequent CS metallization step, a generic zig-zag toolpath with the nozzle oriented normal (orthogonal) to the top surface was used. While this approach provided adequate metallization on horizontal surfaces, it was less effective along the vertical sidewalls and corner regions due to the highly non-orthogonal spray angles. Consequently, reduced particle impact efficiency and coating coverage led to insufficient local metallization and the formation of small voids at the ceramic–CS–WAAM interface. In addition, sharp corners also serve as stress concentrators, and localized damage was observed in the ceramic coating in that region.

Fig. 4 Microstructural analysis of the smart beam: **a** A beam image with regions of interest; **b** Optical microscope image of Section A–A showing the top WAAM–cold spray–ceramic and bottom WAAM interfaces; **c** Schematic of critical interfaces in Section B–B; **d** SEM image of the top WAAM–CS–ceramic interface; and **e** SEM image of the bottom WAAM–epoxy–sensor–ceramic interface

Nevertheless, WAAM was able to over-deposit and completely infill this area due to the small footprint of the defect (less than 1 mm). Aside from this sharp-edge region, the overall structural integrity of the ceramic shielding was preserved throughout both CS metallization and subsequent WAAM over-deposition. As for the interface between the host WAAM layer, FPCB, and embedded sensors, no delamination, cracking, or interfacial damage was observed at the WAAM–FPCB–sensor junction (Fig. 4c). This confirms that the deposition process preserved the structural and functional integrity of the embedded sensors and enabled reliable mechanical bonding between the WAAM layer and the FPCB.

Scanning electron microscopy (SEM, *FEI Versa*) was also performed to analyze the cross-section of Section B–B, with particular focus on two critical interfaces: (1) the top WAAM–CS–ceramic interface and (2) the bottom WAAM–sensor–ceramic interface (Fig. 4c). The SEM image in Fig. 4d shows Interface 1, capturing the upper portion of the embedded sensor package, including the ceramic shielding, the CS-metallized layer, and the top WAAM deposit. The top WAAM region exhibited dense deposition with a high degree of consolidation, and the WAAM–CS interface appeared continuous and well bonded, with no evidence of delamination. This confirms strong metallurgical compatibility between the two layers. In addition, the CS metallization on the ceramic surface exhibited an adherent and conformal coating morphology with a thickness ranging from ∼30 to 91 μm (see Fig. 4d), demonstrating strong coating integrity and effective surface metallization for seamless continuation of WAAM deposition.

Figure 4e focuses on the embedded sensor region, capturing the bottom WAAM–sensor–ceramic interfaces. In this region, the ceramic shielding conformed tightly to the sensor surface, with no evidence of interfacial debonding, thereby providing effective mechanical support and thermal

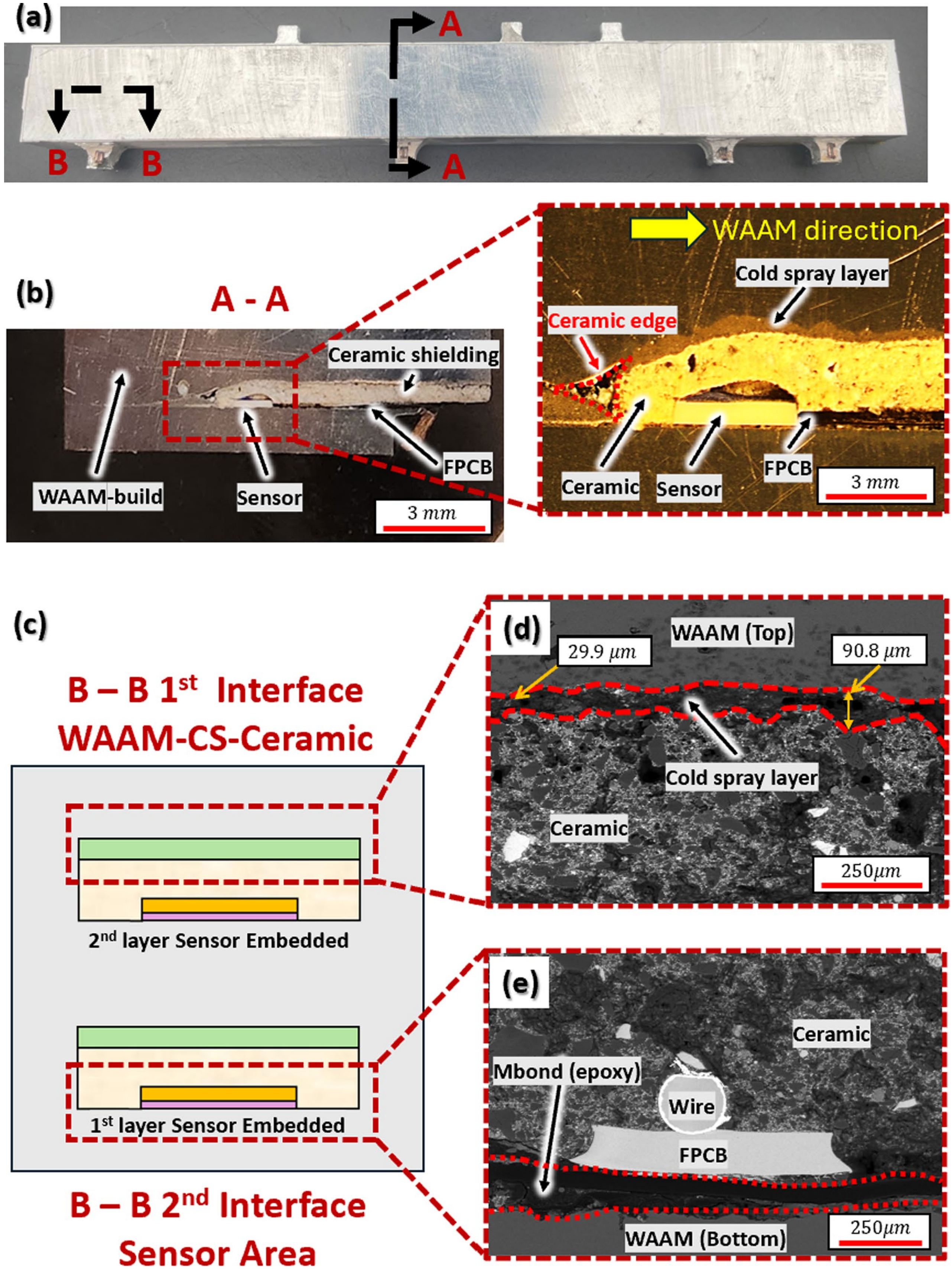
(a)
A
A
B
B
(b)
A - A
Ceramic shielding
WAAM-build
Sensor
FPCB
3 mm
WAAM direction
Cold spray layer
Ceramic edge
Ceramic
Sensor
FPCB
3 mm
(c)
B – B 1st Interface
WAAM-CS-Ceramic
2nd layer Sensor Embedded
1st layer Sensor Embedded
B – B 2nd Interface
Sensor Area
(d)
WAAM (Top)
29.9 μm
90.8 μm
Cold spray layer
Ceramic
250μm
(e)
Ceramic
Mbond (epoxy)
Wire
FPCB
WAAM (Bottom)
250μm

protection. Moreover, the FPCB and its electrode traces preserved their structural integrity, confirming the effectiveness of the ceramic layer in shielding these packaging elements from the excessive heat generated during the WAAM over-deposition. Additionally, the adhesive bonding layer (*M-Bond 610 epoxy*) between the sensor and the bottom WAAM surface remained intact and continuous. This is critical for maintaining reliable sensor contact, particularly for SGs, which require robust bonding to accurately transfer strain from the attached surface.

Overall, the microstructural analyses revealed that the proposed convergent manufacturing approach is robust and reliable, maintaining strong interfacial integrity across all critical interfaces. The absence of delamination confirmed stable mechanical bonding and effective thermal shielding, which validates the proposed approach for embedding sensors within additively manufactured metallic structures. The following sections present the testing and utilization of the developed smart beams under a series of thermal and mechanical evaluations.

4 Structural health monitoring using smart beams

The fabricated smart beams were comprehensively evaluated for structural health monitoring (SHM) through integrated embedded sensing. The evaluations include (i) thermal tests, including steady-state and transient response; (ii) static mechanical tests; (iii) coupled thermo-mechanical tests; (iv) bending-to-fracture tests; and (v) dynamic fatigue tests. All embedded sensors were calibrated prior to testing using reference sensors mounted on the beam surface. The following subsections detail the experimental setups, procedures, and key results for each test.

4.1 Thermal tests

Temperature testing assessed whether the embedded RTDs could accurately sense and track thermal variations within the beam. Two complementary tests were performed: (1) a steady-state test to calibrate the resistance–temperature relationship under equilibrium conditions, and (2) a transient test to evaluate the dynamic response under time-varying heating. Together, these tests established the spatial-temporal sensing capability of the embedded RTD network and informed subsequent thermo-mechanical evaluations.

4.1.1 Steady-state thermal tests

The embedded RTD sensors were first calibrated within a programmable thermal chamber (*Instron, Model: 8801MTB16565*, see Fig. S9, Supporting Information) according to IEC 60751 [38, 39], following Eq. (1), where $R(T)$ is the resistance at temperature T (in °C), R_0 is the nominal resistance at 0 °C, and A and B are $A = 3.908 \times 10^{-3}$ °C^{-1} and $B = -5.775 \times 10^{-7}$ °C^{-2}. During calibration, the beam was freely suspended to minimize conductive heat losses (Fig. 5a, left panel). Four thermocouples (TCs) were attached to the beam surface to provide reference temperature values during calibration, as shown in Fig. 5a. Steady-state measurements were collected at eight temperature setpoints from 50 to 120 °C in 10 °C increments. The mean TC reading at each setpoint was used as the reference temperature. Given the modest temperature range and the small magnitude of B, a linear approximation was adopted as given by Eq. (2), with α and β obtained by least-squares estimation.

$$R(T) = R_0 \left(1 + AT + BT^2\right) \tag{1}$$

$$R(T) \approx \alpha T + \beta \tag{2}$$

Two temperatures (50 and 110 °C) were selected for fitting and the remaining six setpoints were used for validation. Figure 5b shows the change in electrical resistance for each RTD during calibration for embedded sensors in both layers (L1 refers to Layer 1 and L2 to Layer 2), demonstrating consistent and repeatable resistance–temperature behavior across the embedded network. Although RTD2–L2 exhibited a slightly higher nominal resistance corresponding to an offset of approximately 2 Ω (about 0.5 °C temperature bias), this difference was effectively removed by calibrating it against the co-located surface TC, as shown in Fig. 5c. Table 2 summarizes the relative errors with respect to the reference temperatures measured by the TCs, demonstrating excellent agreement.

Following calibration, the beam was heated to 100 °C and held isothermal inside the chamber. All eight embedded RTDs at distinct longitudinal positions were evaluated. As shown in Fig. 5c, the sensors exhibited nearly identical readings, accurately capturing the 100 °C plateau. These results confirm that the embedded RTDs reliably measure internal temperatures and can provide real-time feedback on thermal gradients, localized heating, or potential thermal anomalies under steady-state thermal conditions.

4.1.2 Transient thermal tests

The beam was subjected to transient heating using a programmable ceramic heater (*Watlow, F4T*) mounted on the leftmost surface, as illustrated in Fig. 5d. The details of the experimental setup are provided in Fig. S10 (Supporting Information). The objective was to verify that the embedded

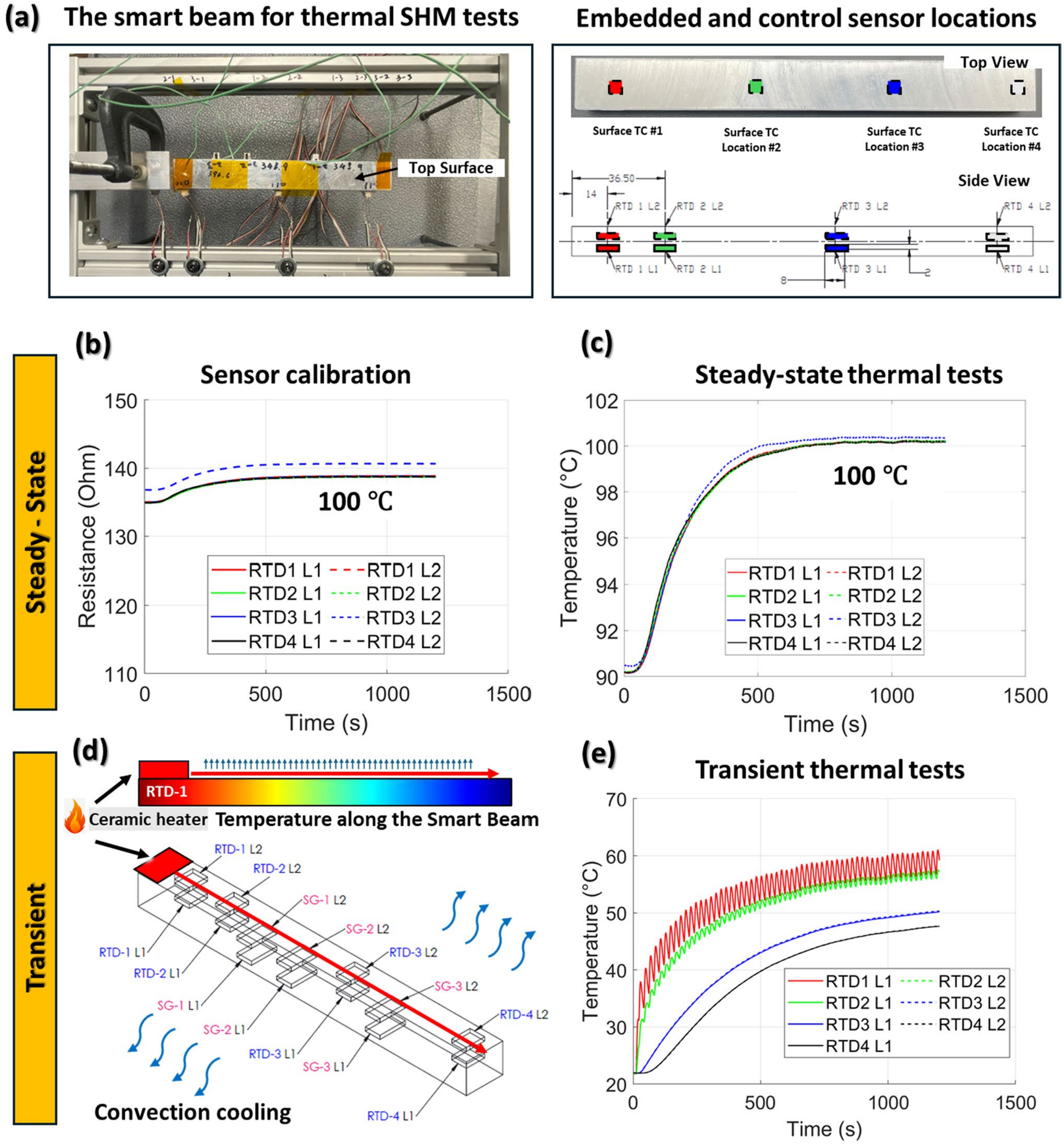

Fig. 5 Thermal tests: **a** Representative image of the beam during thermal testing (left) and the embedded RTD–surface TC sensor network (right); **b** Calibration curves for the embedded RTD sensors; **c** Steady-state thermal test results; **d** Schematic of the transient thermal test; and **e** Transient thermal test results

RTDs can capture rapid temperature changes and sense the time-varying temperature profile on the beam. During testing, a step thermal input was applied on one edge of the beam via the ceramic heater, while the beam was suspended inside a thermally isolated chamber to suppress conductive losses to supports; heat transfer was therefore dominated by in-plane conduction within the beam and residual natural convection to the surrounding air. Heat gradually propagated from the heater side along the beam, producing a progressive temperature increase across the entire span. Each run continued until the temperature readings indicated that

Table 2 Relative calibration errors of embedded RTDs across all temperature setpoints

Temperature (°C)	RTD1 L1 Error (%)	RTD2 L1 Error (%)	RTD3 L1 Error (%)	RTD4 L1 Error (%)
50	0.003	0.003	0.004	0.004
60	0.068	0.069	0.087	0.091
70	0.140	0.139	0.153	0.156
80	0.173	0.170	0.181	0.185
90	0.176	0.167	0.174	0.175
100	0.123	0.115	0.119	0.118
110	0.002	0.002	0.002	0.002
120	0.153	0.147	0.157	0.158
Temperature (°C)	RTD1 L2 Error (%)	RTD2 L2 Error (%)	RTD3 L2 Error (%)	RTD4 L2 Error (%)
50	0.003	0.003	0.004	0.004
60	0.072	0.148	0.095	0.090
70	0.146	1.049	0.162	0.155
80	0.179	0.021	0.186	0.185
90	0.179	0.982	0.194	0.173
100	0.122	0.332	0.137	0.117
110	0.002	0.002	0.002	0.002
120	0.150	0.549	0.184	0.157

the beam had reached steady state, which occurred after approximately 20 min.

Figure 5e shows the temperature measurements from the embedded sensors. RTD-L1 and RTD-L2 exhibited higher temperature magnitudes than the other RTDs due to their proximity to the ceramic heater, as both are located directly beneath the heating source. The noticeable fluctuations in the RTD-L1 readings arise from its immediate exposure to the heater's thermal field, as well as from the feedback-controlled operation of the heating unit, which introduces small oscillations in the local temperature. In contrast, RTD-L2 and downstream sensors exhibited delayed but smoother temperature responses dominated by thermal conduction. The signals from RTD2-L1 and RTD2-L2 were nearly identical, as expected given their small vertical separation within the beam. At farther locations (RTD3 and RTD4 in both layers), temperature variations were attenuated due to convective losses, although both layers showed consistent trends. Overall, the embedded RTDs accurately captured transient temperature changes with strong spatial coherence across the sensor network, demonstrating the sensing capability of the developed smart beams under transient heating conditions. Video S4 (Supporting Information) further showcases the dynamic thermal response sensing behavior of the embedded RTD network during the transient heating process.

4.2 Mechanical tests

Mechanical evaluations were structured into three phases: (1) static loading tests to establish strain-sensing accuracy and robustness, (2) coupled thermo-mechanical loading to assess cross-sensitivity under simultaneous temperature and mechanical loads, and (3) dynamic fatigue loading tests to quantify fatigue performance and determine failure onset.

4.2.1 Static loading tests and strain reconstruction from embedded sensors

The static three-point bending experiments were conducted to verify that the embedded SGs can sense the internal strain field of the smart beam under nominal operating conditions, i.e., within the linear elastic region. In this configuration, the beams were tested under three-point bending in accordance with ASTM E290 [37] using a universal testing machine (*Instron 8801*), as shown in Fig. 6a. Each specimen had a total length of 180 mm and was supported on two rollers positioned 30 mm from each beam end, resulting in an effective support span of $L_b = 120$ mm. A concentrated load was applied at mid-span by the testing machine crosshead, generating a well-defined flexural region at the center of the beam. Displacement control was applied following the displacement-rate/strain-rate relationship (see Sect. 8 in the Supporting Information), and the tests ended at 0.05 mm/mm surface strain or upon specimen fracture. Throughout the loading process, load, mid-span deflection, and strain signals from both surface-mounted and embedded SGs were continuously recorded. The layout of the surface and embedded gauges, and the corresponding strain–time histories under static loading, are shown in Fig. 6b. Details regarding loading control, nominal flexural stress–strain relations, and classical three-point bending formulations are provided in the Supporting Information.

Following the synchronized readings from the surface and embedded SGs under three-point bending, the strain field was reconstructed using beam theory [40], which assumes a linear distribution of bending strain about the neutral axis. Because the distances of the embedded SGs from the neutral axis are known (Fig. 3d), the measured strain values can be mapped to their exact locations within the beam. This enables reconstruction of the through-thickness flexural strain profile and allows direct comparison between embedded and surface measurements.

For a surface gauge located at (x_s, y_s) and an embedded gauge located at (x_e, y_e) within the same symmetric half-span, the measured strains satisfy

$$\frac{\varepsilon_e}{\varepsilon_s} = \frac{M(x_e)\, y_e}{M(x_s)\, y_s} \tag{3}$$

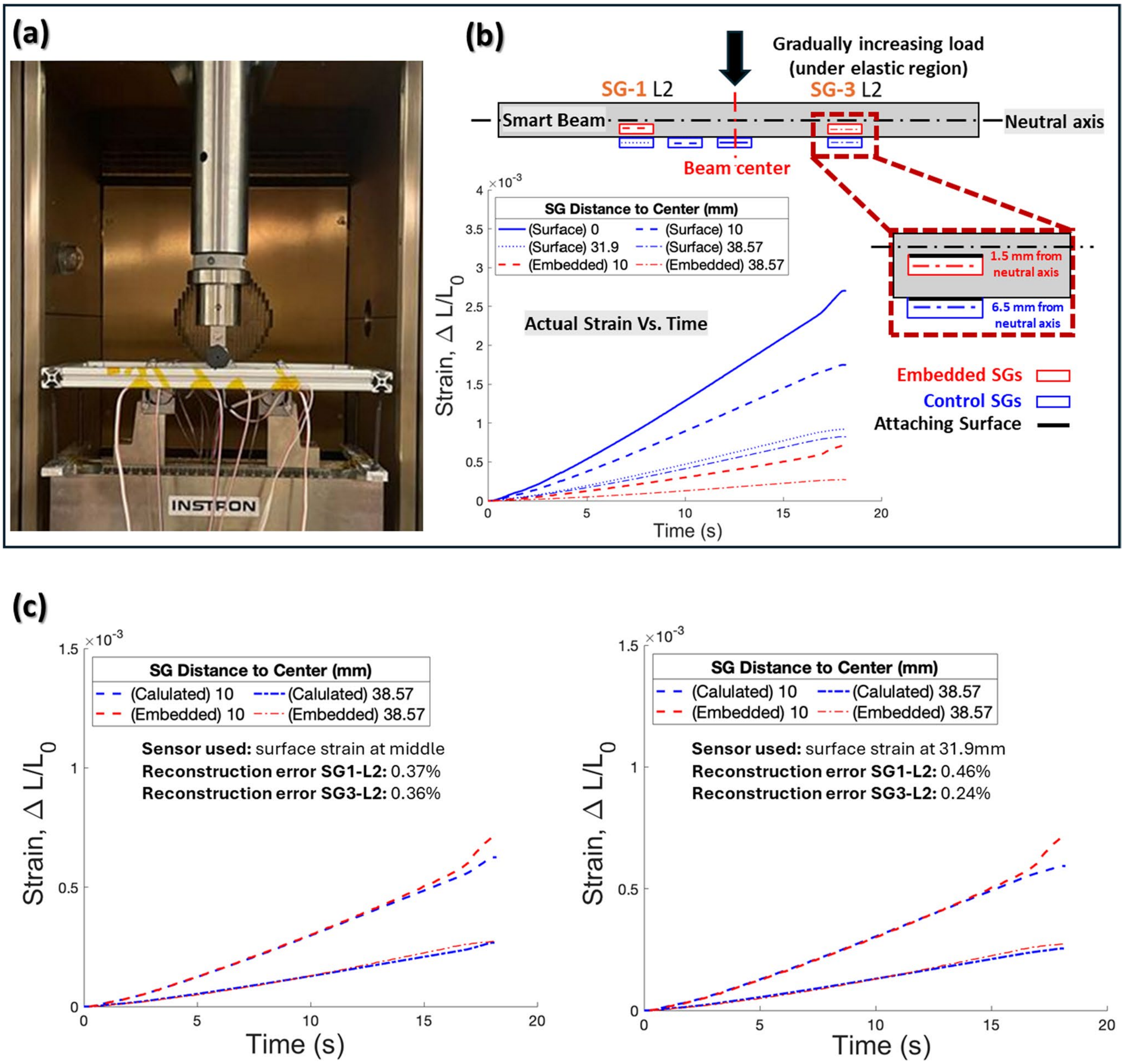

Fig. 6 Static loading and strain reconstruction tests: **a** Experimental setup; **b** Layout of surface and embedded strain sensors across the beam and the corresponding strain–time response under static loading; and **c** Strain reconstruction results based on two distinct control locations

where the bending moment $M(x)$ is given in the Supporting Information (Section S8). Substituting $M(x) = (P_b/2)x$ into Eq. (3) yields

$$\frac{\varepsilon_e}{\varepsilon_s} = \frac{\frac{P_b}{2} x_e y_e}{\frac{P_b}{2} x_s y_s} = \frac{x_e y_e}{x_s y_s} \tag{4}$$

which expresses the strain ratio $\varepsilon_e/\varepsilon_s$ in terms of the spanwise positions and distances from the neutral axis.

In the present study, the spanwise positions x_s and x_e of the surface and embedded SGs are fixed and known from the beam layout, but they are not collocated. The bending-moment difference between the two locations must therefore be accounted for in the depth calibration. Introducing an effective embedded depth y_e^{eff} and replacing y_e in Eq. (3) leads to

$$\frac{\varepsilon_e}{\varepsilon_s} = \frac{M(x_e)\, y_e^{\text{eff}}}{M(x_s)\, y_s} = \frac{x_e y_e^{\text{eff}}}{x_s y_s} \tag{5}$$

from which the effective depth is obtained as

$$y_e^{\text{eff}} = y_s \frac{\varepsilon_e}{\varepsilon_s} \frac{M(x_s)}{M(x_e)} = y_s \frac{\varepsilon_e}{\varepsilon_s} \frac{x_s}{x_e} \tag{6}$$

where y_e^{eff} denotes the calibrated distance of the embedded gauge from the neutral axis.

With the effective depth determined, the embedded sensors were then used for strain-field reconstruction. At each instrumented cross-section, the local bending curvature is defined by

$$\kappa(x) = \frac{\varepsilon_e(x)}{y_e^{\text{eff}}} \tag{7}$$

and, under the Euler–Bernoulli assumption that plane sections remain plane, the longitudinal strain varies linearly with the distance from the neutral axis according to

$$\varepsilon(x, y) = \kappa(x)\, y = \varepsilon_e(x)\, \frac{y}{y_e^{\text{eff}}} \tag{8}$$

In particular, the surface-equivalent strain can be reconstructed from the embedded measurements using

$$\varepsilon_{s,\text{rec}}(x) = \varepsilon_e(x)\, \frac{y_s}{y_e^{\text{eff}}} \tag{9}$$

where $\varepsilon_{s,\text{rec}}(x)$ is the reconstructed surface strain at spanwise position x.

The reconstructed surface strain histories at the instrumented spanwise locations were compared against the strains measured directly by surface SGs. Figure 6c shows representative reconstruction results for two distinct control locations. The resulting strain–time responses exhibited linear and mutually consistent trends over the entire loading range, indicating that the embedded sensors faithfully tracked the flexural deformation. The reconstructed surface strain closely matches the experimental surface SG measurements, with relative errors below 0.5% at both instrumented locations. These results confirm that the calibrated embedded SGs provide reliable through-thickness strain information and enable accurate reconstruction of the flexural strain. Video S5 (Supporting Information) further demonstrates the real-time strain sensing response and deformation monitoring capability of the embedded SG network during applied loading.

4.2.2 Coupled thermo-mechanical tests

To evaluate the sensing fidelity of the embedded sensors, coupled thermo-mechanical tests were conducted in an environmental chamber using a static three-point bending configuration. The beam was positioned on the same 120 mm support span as in the mechanical calibration tests, and quasi-static bending was applied by the testing machine crosshead. The layout of the embedded RTDs and SGs, along with the two surface control gauges, is shown in Fig. 7a. For each isothermal condition (room temperature, approximately 25 °C, and 120 °C), the chamber was brought to the target temperature and held until all RTD readings stabilized. As shown in Fig. 7b, a linear loading–unloading cycle was then applied; the mid-span load was ramped from 0 to peak load over 30 s, held at this level for 120 s, and subsequently unloaded back to 0. The total duration of each loading–unloading cycle was 180 s. This peak load corresponded to a nominal flexural stress of 140 MPa, just below the material's yield stress. Throughout each test, the outputs of all embedded RTDs and SGs, as well as the surface control SGs, were continuously recorded to capture the coupled evolution of temperature and strain.

Fig. 7 Coupled thermo-mechanical tests: **a** Sensor layout; **b** Bending loading profile at room temperature (RT) and 120 °C; **c** Temperature measurements from embedded and surface-mounted RTDs at RT; **d** Surface and embedded SG measurements at RT; **e** Temperature measurements at 120 °C; **f** Surface and embedded SG measurements at 120 °C; **g** Strain reconstruction at RT; and **h** Strain reconstruction at 120 °C

Figure 7c, d show the coupled thermal and mechanical responses at room temperature. During the initial loading stage, the crosshead displacement increased linearly and the strains measured by the SGs rose accordingly. The most highly loaded gauge (SG-1 L2) reached a peak strain of approximately 2×10^{-3}, while the other embedded and surface gauges exhibited proportionally smaller responses, down to roughly 3×10^{-4}. This strain range corresponds to nominal bending stresses below the material's yield strength. A load hold followed, during which the strain levels remained constant, indicating very good stability of the SG measurements under sustained loading. Over the entire testing window, the embedded RTDs indicated that the beam temperature was nearly uniform and varied only slightly (about 1.5%), as shown in Fig. 7d. During the unloading phase, the SG traces closely retraced the loading path and returned to their initial values with negligible residual strain, confirming a linear and reversible response of the SG network.

Figure 7e, f show the coupled thermo-mechanical responses under the elevated-temperature condition of 120 °C. After the chamber reached the target temperature and the system completed the initial thermal stabilization, the crosshead displacement was applied using the same ramp–hold–unload sequence. During the loading ramp, the embedded and surface SG signals changed linearly with time and remained synchronized with the imposed profile: the most highly loaded channel reached a peak strain on the order of 10^{-3}, while the remaining gauges exhibited proportionally smaller amplitudes. During the load-hold interval, the strain traces formed stable plateaus with minimal drift, and upon unloading they returned close to their

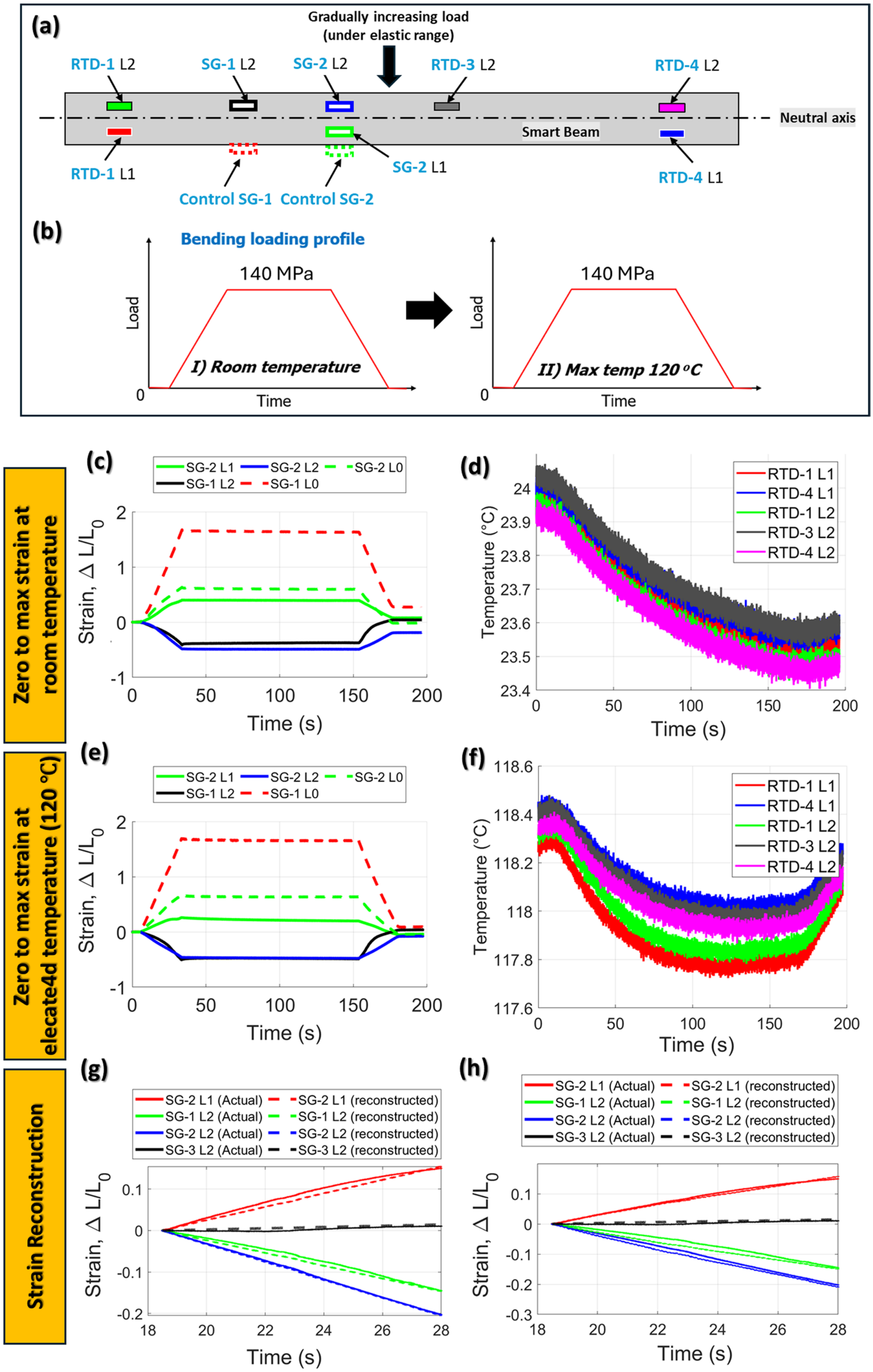
(a)
Gradually increasing load
(under elastic range)
RTD-1 L2
SG-1 L2
SG-2 L2
RTD-3 L2
RTD-4 L2
Neutral axis
Smart Beam
RTD-1 L1
SG-2 L1
RTD-4 L1
Control SG-1
Control SG-2
(b)
Bending loading profile
140 MPa
Load
I) Room temperature
Time
II) Max temp 120 °C
Zero to max strain at room temperature
Zero to max strain at elecate4d temperature (120 °C)
Strain Reconstruction
(c)
(d)
(e)
(f)
(g)
(h)
Strain, Δ L/L0
Time (s)
Temperature (°C)
SG-2 L1
SG-2 L2
SG-2 L0
SG-1 L2
SG-1 L0
RTD-1 L1
RTD-4 L1
RTD-1 L2
RTD-3 L2
RTD-4 L2
SG-2 L1 (Actual)
SG-2 L1 (reconstructed)
SG-1 L2 (Actual)
SG-1 L2 (reconstructed)
SG-2 L2 (Actual)
SG-2 L2 (reconstructed)
SG-3 L2 (Actual)
SG-3 L2 (reconstructed)

initial baselines with negligible residual strain. In parallel, the embedded RTDs maintained a nearly spatially uniform temperature field at 120 °C, with the peak-to-peak spread across sensors remaining within about 0.5% throughout the test, and their temperature trajectories exhibited no measurable dependence on the mechanical loading.

Figure 7g, h present the strain reconstruction results based on the embedded SGs at room temperature and at 120 °C, respectively. In both cases, the reconstructed strain fields closely match the strains measured by the surface control gauges at the corresponding locations. The reconstructed curves nearly overlap the experimental traces throughout the entire loading–unloading cycle, with only minor discrepancies relative to the total strain range. These results demonstrate that the calibration and reconstruction procedures remain valid under coupled thermo-mechanical loading and confirm that the embedded sensor network can reliably capture both temperature and strain fields within the beam across the investigated temperature range.

4.2.3 Bending-to-fracture static tests

To evaluate the ultimate performance and reliability of the embedded sensors, three-point bending tests were extended to fracture. To avoid placing embedded sensors directly beneath the bending indenter, which could lead to locally amplified stress and strain fields and compromise interpretation of the global measured response, the sensor layout within the beam was modified for the static bending tests. Specifically, one RTD and one SG located closest to the mid-span loading axis were removed. As a result, the smart beam specimen used in the static loading experiments contained a total of 12 embedded sensors (see Fig. S5 in the Supporting Information).

Figure 8a, b present the flexural load–deflection curves and flexural stress–strain responses of the tested beams, respectively. Table 3 summarizes the bending-to-fracture results, comparing the flexural modulus (E_{SG}), failure strain, and maximum flexural stress for the baseline and smart-beam specimens. The smart beams exhibited an average flexural modulus of 67.37 GPa, which is comparable to that of the baseline beams (67.73 GPa). However, the smart beams showed an approximately 10.8% reduction in maximum flexural stress relative to the baseline beams. This mechanical debit can be primarily attributed to the presence of embedded sensors and the associated local geometric discontinuities within the beam volume, which act as stress concentration and damage initiation points during bending. In addition, the localized thermal history associated with WAAM deposition around the embedded sensors may introduce residual stress accumulation, further reducing the load-carrying capacity. Despite this modest reduction in maximum flexural stress, the overall mechanical response of the smart beams remains promising, indicating that the proposed manufacturing strategy preserves the structural integrity of the beam while enabling integrated sensing.

Post-test images of the beams in Fig. 8c, d revealed ductile failure localized near mid-span, corresponding to the region of maximum bending stress. The failure was characterized by pronounced plastic curvature and gradual material yielding, consistent with the flexural failure mode typical of three-point bending. Localized delamination was observed along portions of the WAAM layer interfaces, suggesting the onset of interfacial separation under high bending strains. However, these regions remained confined and did not propagate catastrophically, demonstrating that the metal–ceramic–sensor architecture retained overall structural integrity up to failure.

4.2.4 Dynamic loading tests

To evaluate the dynamic-loading performance of the smart beams, a three-point bending low-cycle fatigue test was performed. Since the fatigue tests were intended to assess the overall structural health behavior under cyclic loading rather than localized stress-concentration effects, the sensor density in the high-stress contact regions was reduced. Specifically, all sensors located near the bending indenter and supporting rollers were removed. The final configuration consisted of a six-sensor network (3 RTDs + 3 SGs) distributed within two internal layers of the beam, as shown in Fig. 9a. In this configuration, two SGs and one RTD were placed on the compression side, while two RTDs and one SG were positioned on the tension side. A detailed technical drawing of the beam and corresponding sensor layout is provided in Fig. S6 (Supporting Information). Dynamic loading tests were carried out using a programmable fatigue testing system (*Instron No. 8801MTB16565*), shown in Fig. 9b. Cyclic loading was applied over a nominal stress range of 20–200 MPa at a load frequency of 5 Hz (Fig. 9c). The beam was positioned identically to the static-loading setup, and temperature and strain data were continuously recorded until the onset of fatigue damage and eventual fracture. Fig. 9d presents side-by-side post-test images of the baseline and smart beams. In both cases, fracture occurred at mid-span, the region of maximum bending stress, confirming that the embedded sensor network did not alter the fundamental failure mode.

Table 4 compares three baseline–smart-beam pairs, with all differences computed relative to the mean fatigue life of the baseline beams. The smart beams exhibited a fatigue life approximately 20% lower than the baseline beams (smart beam: 250k cycles; baseline beam: 312k cycles). This reduction reflects the presence of local stress concentrations

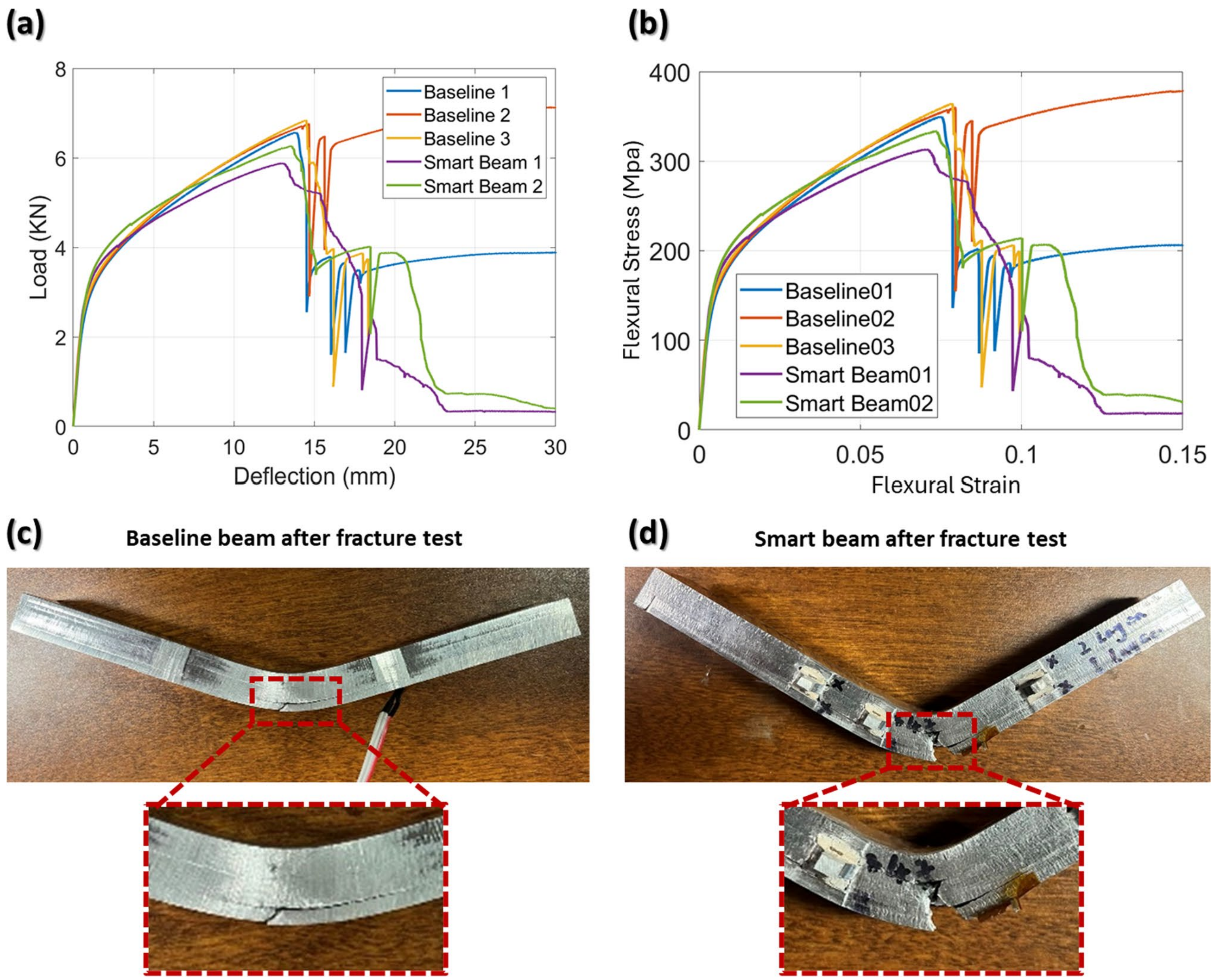

Fig. 8 Bending-to-fracture test results: **a** Deflection–load plot of baseline beams and smart beams; **b** Flexural stress–strain plot of the beams; **c** Post-test images of a baseline; and **d** smart beams

Table 3 Mechanical properties comparison of baseline (pristine) and smart beams

Sample ID	Flexural Modulus, E_{SG} (GPa)	Failure Strain	Max. Flexural Stress (MPa)
Baseline 1	68.15	0.0747	349.56
Baseline 2	68.86	0.0794	380.34
Baseline 3	66.19	0.0781	364.44
Mean ± std	**67.73 ± 1.38**	**0.0774 ± 0.0020**	**364.78 ± 15.39**
Smart Beam 1	69.69	0.0731	334.63
Smart Beam 2	65.05	0.0710	316.37
Mean ± std	**67.37 ± 3.28**	**0.0721 ± 0.0010**	**325.50 ± 12.91**

These values represent the averages and standard deviations.

associated with the embedded sensors. Figure 9e, f summarize the RTD and SG responses over the full dynamic fatigue test, with the dashed boxes highlighting the near-failure interval. Throughout cycling, all sensing channels remained continuous and functional. The RTDs exhibit only a slow, near-monotonic resistance drift of about 0.1 Ω across the test, corresponding to a temperature change of about 0.3 °C. Importantly, the RTD traces remain smooth during the late-stage zoomed region, indicating that fatigue loading does not introduce noticeable electrical artifacts or load-dependent cross-sensitivity in the temperature measurements.

In parallel, the strain sensors in Fig. 9f capture the expected cyclic response to the applied dynamic bending while also revealing a gradual baseline shift as damage accumulates. Specifically, the L1 gauge (SG-2 L1) progressively shifts toward higher tensile strain, whereas the L2 gauges (SG-2 L2 and SG-1 L2) exhibit steadily increasing

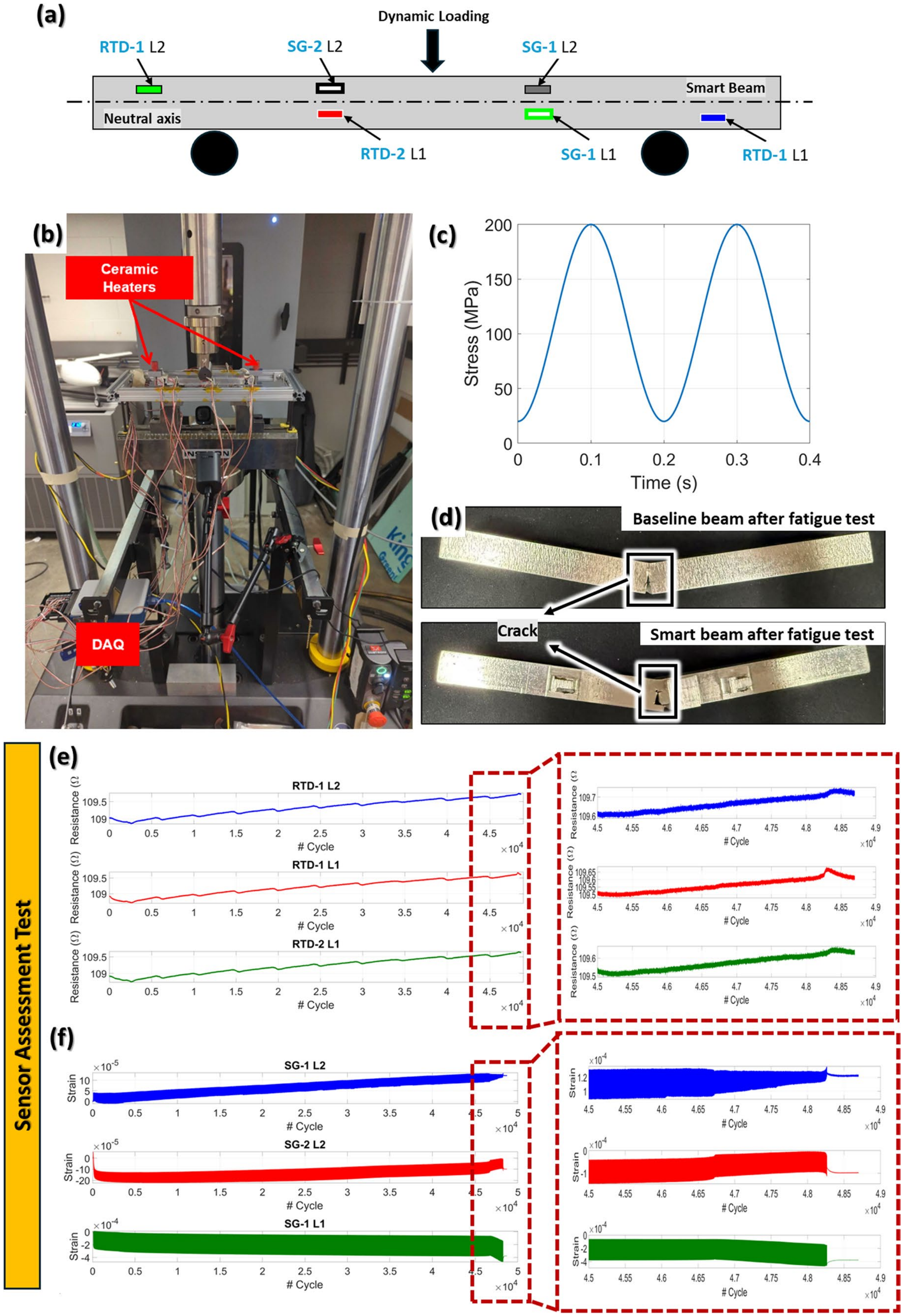
(a)
Dynamic Loading
RTD-1 L2
SG-2 L2
SG-1 L2
Smart Beam
Neutral axis
RTD-2 L1
SG-1 L1
RTD-1 L1
(b)
Ceramic Heaters
DAQ
(c)
Stress (MPa)
Time (s)
(d)
Baseline beam after fatigue test
Crack
Smart beam after fatigue test
Sensor Assessment Test
(e)
RTD-1 L2
RTD-1 L1
RTD-2 L1
Resistance (Ω)
Cycle
(f)
SG-1 L2
SG-2 L2
SG-1 L1
Strain
Cycle

Fig. 9 Dynamic loading tests: **a** Sensor layout and loading configuration; **b** Experimental setup; **c** Loading cycle profiles; **d** Fracture behaviors of baseline and smart beams under dynamic loading; **e** RTD response during dynamic loading with a distinct signal change at fracture; and **f** SG response during dynamic loading with a distinct signal change at fracture

compression, i.e., their mean strain becomes more negative with cycle count. This divergence between the tensile-side and compressive-side trends is consistent with subtle progressive deformation and stiffness degradation under repeated loading, which manifests as a slow redistribution of curvature and local strain levels rather than an abrupt change prior to fracture. At failure, both RTD and SG traces show a clear step change in their readouts yet remain readable immediately afterward, confirming preserved sensor operability and robust signal integrity under high-cycle dynamic loading up to and through fracture.

5 Discussion

Table 5 quantitatively summarizes the key findings and experimental observations discussed throughout this study. Notably, low sensor measurement errors ($< 2.5\%$) were achieved, demonstrating the reliability and effectiveness of the proposed convergent manufacturing approach for SMSs. Despite these promising results, several aspects should be further investigated to enhance sensing performance, structural durability, and long-term operational reliability:

1. Heterogeneous material systems (i.e., metal, polymer sensor packaging, and ceramic shielding) and their interfaces may introduce stiffness and coefficient of thermal expansion (CTE) mismatches, potentially generating residual stresses and affecting local strain transfer to the embedded SGs. Future work should therefore focus on material and packaging optimization, thermo-mechanical modeling, and interface characterization to mitigate these effects and further improve sensor fidelity and reliability.
2. Non-orthogonal alignment of the CS nozzle relative to the target surface limited metallization coverage at sharp edges and corners of the ceramic layer, leading to localized coating discontinuities and void formation at the ceramic–CS–WAAM interface. Future work should focus on intelligent toolpath planning to improve coating uniformity and interfacial integrity in complex geometries, particularly for sensor embedding in non-linear structures relevant to aerospace, energy, and advanced structural applications.
3. The integration of robotic subtractive manufacturing and direct-write or 3D-printed ceramic deposition with robotic WAAM within a single manufacturing cell could establish a one-station convergent manufacturing platform. Such integration would reduce part handling, improve additive–subtractive process registration, enable more consistent and controllable ceramic deposition, and support the scalable fabrication of complex SMSs. Consequently, it could further enhance the fatigue life and long-term reliability of sensor-embedded SMS.

6 Conclusions

This work developed a convergent manufacturing pathway for fabricating smart metallic structures with embedded sensors and subsequently validated their reliability for structural monitoring applications. The approach employed a process workflow comprising WAAM, subtractive machining, ceramic shielding, cold spray metallization, and WAAM over-deposition. The key findings are outlined as follows:

- The developed approach enabled reliable embedding of multi modal (temperature + strain) sensors within WAAM-built Al5356 structures without significantly compromising interfacial integrity across the heterogeneous material interfaces.
- Embedded RTDs demonstrated high accuracy under both steady-state and transient heating conditions, maintaining temperature errors below 2.2%.
- Embedded SGs provided consistent strain measurements, deviating by less than 2.5% from surface-mounted reference sensors.
- Bending-to-fracture tests showed that the smart beams retained more than 89% of the mechanical strength and approximately 80% of the fatigue life of baseline beams. The embedded sensors and interfacial layers remained intact through ductile fracture, confirming the mechanical robustness of the embedded sensor network and reliable signal transfer up to failure.
- Sensor durability tests under combined dynamic loading and thermal cycling demonstrated that both the SGs and RTDs remained fully functional up to the point of fatigue failure, confirming the effectiveness and reliability of the sensor protection strategy.

Collectively, the results demonstrate that the proposed convergent manufacturing approach establishes a viable pathway for next-generation SMS. Future work may extend this approach to additional sensor modalities, such as piezoelectric, accelerometer, and fiber-optic sensors, and explore passive or wireless sensing to broaden the operational envelope of SMS systems. Simulation-assisted sensor-network design and data-driven methods can further enhance SHM

Table 4 Low-cycle fatigue life comparison between baseline beams and smart beams

Sample ID	Fatigue Life N_f (cycles)	Diff. wrt mean N_f (%)
Baseline 4	383K	+22.6
Baseline 5	217K	−30.5
Baseline 6	337K	+7.9
Mean (Baseline)	**312K**	–
Smart Beam 3	260K	−16.8
Smart Beam 4	211K	−32.4
Smart Beam 5	278K	−11.0
Mean (Smart beam)	**250K**	–

These values represent the averages and standard deviations.

Table 5 Summary of sensor measurement errors (relative to surface-mounted control gauges) and the corresponding mechanical debits (relative to baseline beams)

Measurement	Parameter	Difference (%)
Strain	Max. strain at room temperature (25 °C)	< 2.5
	Max. strain at 120 °C	< 0.8
Temperature	Calibration at room temperature (25 °C)	< 0.98
	Field reconstruction at room temperature	< 0.78
	Calibration at 120 °C	< 0.98
	Field reconstruction at 120 °C	< 2.2
Mechanical property	Flexural modulus	< 4.3
	Strain to failure	< 8
	Max. flexural stress	< 11
	Fatigue life cycle	< 20

capabilities and support predictive maintenance of complex structural components.

Supplementary Information The online version contains supplementary material available at https://doi.org/10.1007/s40964-026-01813-6.

Acknowledgements This work was funded by the Defense Advanced Research Projects Agency (DARPA) SENSE: Structural Evaluation through Non-contact Sensor Embedding program (HR00112490367) between DARPA and Rensselaer Polytechnic Institute (RPI). The authors gratefully acknowledge DARPA for funding this work and sincerely thank Dr. Andrew Detor, Dr. Alireza Kermani, and Dr. Paul Witherell for their valuable guidance and feedback throughout the effort. Internal funding from RPI is also acknowledged. The authors also thank Sazidur R. Shahriar, Kyle Young, Petros Spiliopoulos, James Schure, Jonah Mahe, Michael Goldshteyn, Daniel Flynn, Joseph Brewster, and Joyce Ke for their support.

Author contributions J. R.: Conceptualization, Data curation, Investigation, Methodology, Validation, Visualization, Writing—original draft. S. H.: Conceptualization, Data curation, Investigation, Methodology, Validation, Visualization, Writing—original draft. S. R.: Investigation, Methodology, Validation, Writing—original draft. P. Z.: Investigation, Methodology, Validation. Y. F.: Investigation, Methodology, Validation. B. V.:Investigation, Methodology. G. S.: Conceptualization, Supervision. J. W.: Conceptualization, Supervision. S. M.: Conceptualization, Supervision. J. S.: Conceptualization, Methodology, Validation, Funding acquisition, Supervision. F. K.: Conceptualization, Data curation, Investigation, Methodology, Validation, Funding acquisition, Supervision, Writing—original draft. S. A.: Conceptualization, Data curation, Investigation, Methodology, Validation, Funding acquisition, Supervision, Writing—original draft. All authors reviewed the manuscript.

Data availability No datasets were generated or analysed during the current study.

Declarations

Conflict of interest The authors declare the following competing financial interest: A patent application related to the materials and process for smart metallic structures has been submitted to the U.S. patent office for consideration and is currently pending.

References

1. Wang B, Lee TL, Qin Y (2023) Advances in smart materials and structures. Materials 16(22):7206
2. Gomez-Cabrera A, Escamilla-Ambrosio PJ (2022) Review of machine-learning techniques applied to structural health monitoring systems for building and bridge structures. Appl Sci 12(21):10754
3. Li X, Prinz F (2003) Embedded fiber Bragg grating sensors in polymer structures fabricated by layered manufacturing. J Manuf Process 5(1):78–86
4. Li X, Fritz B, Prinz (2000) Embedding of fiber optic sensors in layered manufacturing 314
5. Laurent ML, Marquis GE, Gonzalez M, Tansel I, Tosunoglu S (2025) Embedded sensing in additive manufacturing metal and polymer parts: a comparative study of integration techniques and structural health monitoring performance. Algorithms 18(10):613
6. Šakalys R, O'Hara C, Kariminejad M, Weinert A, Kadivar M, Zluhan B, McAfee M, McGranaghan G, Tormey D, Raghavendra R (2024) Embedding a surface acoustic wave sensor and venting into a metal additively manufactured injection mould tool for targeted temperature monitoring. Int J Adv Manuf Technol 130(11):5627–5640
7. Scarselli G, Nicassio F (2025) Machine learning for structural health monitoring of aerospace structures: A review. Sensors 25(19):6136
8. Defense Advanced Research Projects Agency (DARPA). Structural evaluation program. https://www.darpa.mil/research/programs/structural-evaluation, 2024. Accessed: 2025-02-14
9. Ferreira PM, Machado MA, Carvalho MS, Vidal C (2022) Embedded sensors for structural health monitoring: methodologies and applications review. Sensors 22(21):8320
10. Lovett E, Hammond M, Seyfi N, Golestaneh AF, Cichella V, Lamuta C (2025) A review on sensor technologies, control approaches, and emerging challenges in soft robotics. Adv Robot Res. https://doi.org/10.1002/adrr.202500085
11. Allady A, Maini R (2023) Embedded sensor technology application for offshore energy industry. SNAME Offshore Symposium, p. D011S003R002. SNAME
12. Kong H, Huang W, Zhang Y, Lin J, Yang J, Zhang Z (2025) Energy absorption behavior of AL/CFRP hybrid tubes under tearing trigger mechanism. Compos B Eng 304:112679
13. Juhasz M, Tiedemann R, Dumstorff G, Walker J, Plessis AD, Conner B, Lang W, MacDonald E (2020) Hybrid directed energy deposition for fabricating metal structures with embedded sensors. Addit Manuf 35:101397
14. Abdollahi-Mamoudan F, Ibarra-Castanedo C, Maldague XPV (2025) Non-destructive testing and evaluation of hybrid and

advanced structures: a comprehensive review of methods, applications, and emerging trends. Sensors 25(12):3635
15. Armstrong M, Mehrabi H, Naveed N (2022) An overview of modern metal additive manufacturing technology. J Manuf Process 84:1001–1029
16. Rahman S, Akin S, Ren J, Zhou P, Kopsaftopoulos F, Samuel J (2026) Additively manufactured smart metallic structures with embedded sensing: a review. Progr Addit Manuf 11:1–42
17. Lee MS, Lee J, Sung H, Choe J, Son HJ, Yun J, K-b Kim M, Kim SWL, Yang S et al (2020) Embedding sensors using selective laser melting for self-cognitive metal parts. Addit Manuf 33:101151
18. Hossain MS, Gonzalez JA, Hernandez RM, Shuvo MAI, Mireles J, Choudhuri A, Lin Y, Wicker RB (2016) Fabrication of smart parts using powder bed fusion additive manufacturing technology. Addit Manuf 10:58–66
19. Tomaz I, Mhurchadha SMU, Marques S, Quinn P, Funke H, Birkholz F, Zietzschmann S, Raghavendra R (2021) The development of a smart additively manufactured part with an embedded surface acoustic wave sensor. Addit Manuf Lett 1:100004
20. Zhong S, Zhao K, Nguyen DS, Zhu Q, Zou R, Wu Z, Wang Q, Zhang G, Ma G, Li Y (2025) Improving high temperature resilience of fiber sensor embedded smart components through laser shock peening. Opt Expr 33(7):16003–16013
21. Nuñez L III, Sabharwall P, van Rooyen IJ (2023) In situ embedment of type k sheathed thermocouples with directed energy deposition. Int J Adv Manuf Technol 127(7):3611–3623
22. Hyer HC, Sweeney DC, Petrie CM (2022) Functional fiber-optic sensors embedded in stainless steel components using ultrasonic additive manufacturing for distributed temperature and strain measurements. Addit Manuf 52:102681
23. Ramanathan AK, Gingerich MB, Headings LM, Dapino MJ (2022) Metal structures embedded with piezoelectric pvdf sensors using ultrasonic additive manufacturing. Manuf Lett 31:96–100
24. Zhao J, Dong W, Hinds T, Li Y, Splain Z, Zhong S, Wang Q, Bajaj N, To A, Ahmed M et al (2023) Embedded fiber Bragg grating (fbg) sensors fabricated by ultrasonic additive manufacturing for high-frequency dynamic strain measurements. IEEE Sens J 24(3):2853–2862
25. Feldhausen T, Yelamanchi B, Gomez A, Plessis AD, Heinrich L, Saleeby K, Fillingim K, Post B, Love L, Cortes P et al (2023) Embedding ceramic components in metal structures with hybrid directed energy deposition. Int J Adv Manuf Technol 125(9):4425–4433
26. Wei C, Zhang Z, Cheng D, Sun Z, Zhu M, Li L (2021) An overview of laser-based multiple metallic material additive manufacturing: from macro-to micro-scales. Int J Extr Manuf 3(1):012003
27. Al-Baradoni N, Groche P (2022) Sensor-integrated structures in mechanical engineering: challenges and opportunities for mechanical joining processes. Prod Eng Res Devel 16(2):423–434
28. Huang S, Ren J, Zhou P, Rahman S, Young K, Rahman SS, Mishra S, Samuel J, Kopsaftopoulos F, Akin S (2025) A multifunctional smart metal beam with sub-surface embedded sensors for real-time structural health monitoring. Struct Health Monitor, https://doi.org/10.12783/shm2025/37491
29. Zhou P, Ren J, Schure JS, Huang S, Rahman S, Mishra S, Samuel J, Akin S, Kopsaftopoulos F (2025) A novel shm architecture for self-aware structures. Structural Health Monitoring, Embedded piezoelectric sensing for metallic components, 2025
30. Treutler K, Wesling V (2021) The current state of research of wire arc additive manufacturing (waam): a review. Appl Sci 11(18):8619
31. Zuo X, Lv Z, Wang Y, Chen X, Qi W (2025) Microstructural organization and mechanical properties of 5356 aluminum alloy wire arc additive manufacturing under low heat input conditions. Metals 15(2):116
32. He H, Lu C-L, Ren J, Dhar J, Saunders G, Wason J, Samuel J, Julius A, Wen JT (2025) Open-source software architecture for multi-robot wire arc additive manufacturing (waam). Applicat Eng Sci 22:100204
33. Lu C-L, He H, Ren J, Dhar J, Saunders G, Julius A, Samuel J, Wen JT (2025) Multi-robot scan-n-print for wire arc additive manufacturing. ASME Lett Transl Robot 1(1):011003
34. Omega D Thin film platinum rtd element (5 packs). https://www.dwyeromega.com/en-us/thin-film-platinum-rtd-element-5-packs/p/5RTD-F3100. Accessed: 2025-02-14
35. Omega D Biaxial 90° t-rosette strain gauges (transducer quality), model sgt-2-350-xy43. https://www.dwyeromega.com/en-us/biaxial-90-t-rosette-strain-gauges-with-transducer-quality/SGT-2-ELEMENT90/p/SGT-2-350-XY43. Accessed: 2025-02-14
36. Micro-Measurements. M-bond 610 strain gage adhesive – technical data sheet. Micro-Measurements datasheet. Accessed: 2025-02-14
37. ASTM International. Astm e290-14: Standard test methods for bend testing of material for ductility. ASTM International Standard, 2014. https://www.astm.org/e0290-14.html
38. International Electrotechnical Commission (2022) Iec 60751: Industrial platinum resistance thermometers and platinum temperature sensors. International Standard. Specifies resistance–temperature relationship and tolerance classes for platinum RTDs
39. Otomański P, Pawłowski E, Szlachta A (2025) In situ evaluation of the self-heating effect in resistance temperature sensors. Sensors 25(11):3374
40. James M, Gere, Barry J, Goodno (2001) Mechanics of materials 5th, vol 780. Brooks Cole

Authors and Affiliations

Jinhan Ren[1] · Shinan Huang[1] · Sazedur Rahman[1] · Peiyuan Zhou[1] · Yiming Fan[1] · Brandon Villanueva[1] · Glenn Saunders[1,2] · John Wen[2,3] · Sandipan Mishra[1,2] · Johnson Samuel[1,2] · Fotis Kopsaftopoulos[1,2] · Semih Akin[1,2]

✉ Johnson Samuel
SAMUEJ2@rpi.edu

✉ Fotis Kopsaftopoulos
kopsaf@rpi.edu

✉ Semih Akin
akins@rpi.edu

Jinhan Ren
RENJ2@rpi.edu

Shinan Huang
HUANGS12@rpi.edu

Sazedur Rahman
rahmas5@rpi.edu

Peiyuan Zhou
zhoup2@rpi.edu

Yiming Fan
fany5@rpi.edu

Brandon Villanueva
villab@rpi.edu

Glenn Saunders
saundg@rpi.edu

John Wen
wenj@rpi.edu

Sandipan Mishra
MISHRS2@rpi.edu

1 Department of Mechanical, Aerospace, and Nuclear Engineering, Rensselaer Polytechnic Institute, Troy, USA

2 Rensselaer Polytechnic Institute, Center for Smart Convergent Manufacturing Systems (CSCMS), Troy, USA

3 Department of Electrical, Computer, and Systems Engineering, Rensselaer Polytechnic Institute, Troy, USA